41

# Qualitative formability assessment tools for blank development in press forming

ISU
1996
P56
c. 1

by

Helder José Brandão Pinheiro

A thesis submitted to the graduate faculty

in partial fulfillment of the requirements for the degree of

MASTER OF SCIENCE

Department: Mechanical Engineering

Major: Mechanical Engineering

Major Professor: James H. Oliver

Iowa State University

Ames, Iowa

1996

Graduate College
Iowa State University

This is to certify that the Master's thesis of

Helder José Brandão Pinheiro

has met the thesis requirements of Iowa State University

Signatures have been redacted for privacy

# TABLE OF CONTENTS

# LIST OF FIGURES

# ACKNOWLEDGEMENTS

This research was supported by the National Science Foundation (grant number DMI/ 9258114) and the Iowa Center for Emerging Manufacturing Technology. I am very grateful for this support.

I thank my parents and my sister back in Portugal for their support. They were always very patient and understanding even when I didn't write home frequently. I wish to thank my advisor, Dr. James Oliver, for all his help and for being a good friend. I also thank my friends Ash, Eric, Dave, Maria, Dan, John and Perry.

I finally thank my Wiltgen family and a very sweet soon-to-be architect called Beverly for her constant encouragement and for always believing in me.

# 1. INTRODUCTION

The recent advancements in computational methods along with faster computers have led many industries to use computer models and simulations as fundamental tools in design and manufacturing. In fact, many processes can only be studied accurately or developed with simulating procedures and mathematical algorithms. Among such processes is press forming, one of the most widely used methods in many industries.

During press forming a punch with a defined geometrical shape deforms an initially flat sheet of metal against a die until its final deformed state. A detailed study and analysis of this process is very complex since it depends on material properties, friction between the sheet and the punch and forces of contact among other variables. Due to this fact, predicting results has been left up to design and tooling engineers with experience in the field and trial-and-error procedures are also employed.

The initial procedure in the process of press forming is called blank development. The blank is the initial flat sheet used to develop the final shape. The designer has to predict the approximate amount of material needed as well as the required shape of the blank in order to ensure a smooth deformation without wrinkling or thinning during press forming. This is influenced by the draw binder ring, which is placed outside the trim line, i.e., the boundary between the formed surface and surrounding scrap material. In order to locate the trim line, the designer must determine the boundary of the area on the blank which is affected by the forming process. The developed blank is also used for press forming layout, punch contact analysis and to give an indication of material flow.

The redesign of a product that fails in production can be very expensive in terms of time and capital investment, and so it would be useful for the designer to have some kind of manufacturing feedback in the early stages of the design process. The technique presented in this research is intended to do just that. It is far less demanding in terms of computation than other techniques such as finite element methods and can therefore be used readily as an interactive tool to provide qualitative information about formability and surface construction.

This thesis introduces improved methods for determining the approximate blank shape for the design surface. A new alternative mapping procedure is introduced that can be used for more complex surfaces. Simple cases of non-developable surfaces are addressed and then a new algorithm is used to handle more realistic shapes. A volume conservation technique for mapping is presented as an extension of a previous studied constant area transformation algorithm. A methodology for calculating surface geometric strains is presented which is used as a validation tool in the determination of the blank.

Algorithm implementations were written in C++ on Silicon Graphics workstations using Open Inventor for the graphical interface and ViewKit, a X/Motif based toolkit for the user interface.

# 2. RELATED RESEARCH

This chapter introduces some of the more significant achievements in the modeling of sheet metal forming processes and in the area of blank development.

## 2.1 Modeling of Sheet Metal Forming Processes

Due to the fact that sheet metal forming involves very complex interactions, it has been a challenge to develop accurate models that describe the process. The pioneering work done by Sachs [1] on the analysis of a deep drawn cup with a hemispherical punch motivated a series of studies such as Swift [2] and Hill [3], that improved significantly the understanding of sheet metal forming.

Since then many researchers have concentrated in several areas of the forming process such as the studies of material behavior [4], forming limit diagrams [5, 6, 7], constitutive equations for sheet forming analysis [8, 9, 10] and plastic flow [11].

Most of these studies have included both theoretical and experimental aspects aimed at predicting material behavior, states of stress and strain, and failure or wrinkling, and they focused on the analysis of the process rather than the designing procedure.

Numerical methods such as the finite element method have also been applied to model sheet metal forming. Sheet metal deformation has been studied for several shapes and situations with finite element methods in order to analyze or predict results [12, 13, 14]. Other techniques such as the slip line field approach [15] and the upper bound approach [16] have also been applied.

Several companies mostly in the automobile and aerospace industries have developed modified finite element methods suited to their specific needs for the design and/or analysis of several products [17, 18].

## 2.2 Blank Development

The blank development of non-developable surfaces has been studied mostly with the aid of finite element methods [19]. Non-developable surfaces are part of a family of surfaces that have non-zero Gaussian curvatures and cannot be generated by bending a plane without some distortion [20]. The need for tools that can produce approximate answers to some of the questions raised by designers has led to the development of alternative ways to study the blank development process. Several studies for simple shapes have been done by Gerdeen and Chen [21] in which mathematical relationships were developed to describe thickness variations throughout the piece. Karima has studied the blank development for drawn parts using a slip-line field approach [15].

Chu. et al. introduced a mapping strategy that takes into account only geometrical information [22]. Blount and Stevens have also applied this method to the study of forming of heavy gauge metal [23]. Chu's approach motivated the work done by Nair [20] from which the research presented in this thesis originates.

## 2.3 Research Background

The presented research is motivated by the studies done by Nair [20]. What follows is a brief introduction to the constant area transformation technique developed by Nair.

The fundamental characteristics of Nair's algorithm are:

- A reversal of the forming process from the formed to the unformed state.

• A geometric conservation of area between the two states.

Nair uses a uniform grid of points from a polygonal surface model to describe the surface. Any three adjacent non-colinear vertices form the elemental area entities used for the conservation of area between the formed and undeformed states. The basis of the algorithm is the following:

• Given a triangle $T(V_i, V_j, V_k) \in E^3$ with area $A$ and corresponding projected locations of two vertices $V'_i$ and $V'_j$ in $E^2$, a family of triangles $T(V'_i, V'_j, V'_k)$ of area $A$ is defined by the area locus $l$ of the point $V'_k \in E^2$ which is a line parallel to $V'_iV'_j$ at a distance $h = 2A/\left|V'_iV'_j\right|$ from $V'_iV'_j$. (See Figure 2.1.)

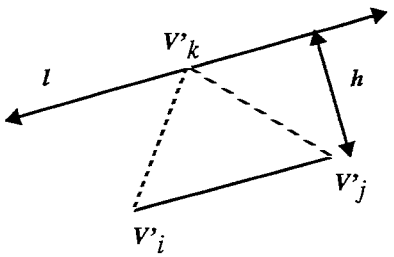


**Figure 2.1 Locus of the third vertex of a family of constant area triangles [2**

• Given two adjacent triangles $T_a(V_i, V_j, V_l)$ and $T_b(V_k, V_i, V_l) \in E^3$ and corresponding projected locations of any three of these vertices in a plane in $E^2$, say $V'_i, V'_j$ and $V'_k$, as shown in Figure 2.2, if the unknown common vertex $V_l' \in E^2$ is located at the intersection of area loci $l_a \leftarrow T_a\left(V'_i, V'_j, V'_l\right)$ and $l_b \leftarrow T_b\left(V'_k, V'_i, V'_l\right)$, then

$$Area\left(V_i, V_j, V_l\right) = Area\left(V'_i, V'_j, V'_l\right) \text{ and}$$
$$Area\left(V_k, V_i, V_l\right) = Area\left(V'_k, V'_i, V'_l\right) \tag{2.1}$$

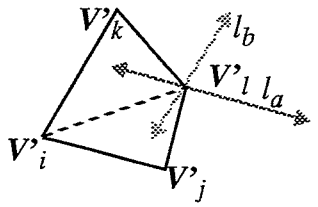


**Figure 2.2 Area conservation principle [20].**

In order to initialize the algorithm, the position of one vertex on the blank is necessary. Nair assumes the blank plane to be the global XY plane and that the punch travels parallel to the Z-axis. The point with the largest Z-value is then taken as the seed to the algorithm by projecting it directly onto the blank plane. The mapping proceeds then concentrically from the starting point.

Some of the assumptions and/or limitations of Nair's algorithm are:

- The ideal process is assumed, i.e., the thickness is assumed to remain constant throughout the forming process.
- For geometrically complex surfaces, the assumption of having only one starting point that retains the same X and Y coordinates is too simplistic.

These considerations have led to further investigations on Nair's technique. The results are presented in the following chapters of this thesis.

# 3. MULTI-PEAK MAPPING

Nair's formulation is limited, in terms of realistic results, to the mapping of simple surfaces. The algorithm encounters problems when applied to more complex shapes with regions of high curvature, large indentations, etc. Also, the assumption that the starting point remains fixed, i.e., it maintains its X and Y coordinates, proves to be a simplistic approach. In many cases there might be several starting points with none of them maintaining its XY position. These concerns led to the investigation of several methods for the application of the constant area transformation to more detailed and complex shapes. This chapter presents the studies done on the topic.

## 3.1 Merging Fronts

For the cases where the geometrical shape has more than one point with a maximum Z-value (see section 2.3) the logical and simple approach to take is to start the algorithm at those points simultaneously. The mapping would then proceed concentrically from those points. Nair addresses briefly the possibility of having a situation where two or more fronts merge [20], where cases would arise with five, six, or even seven neighbor vertices already mapped. This method, however proves to be unusable due to a problem of overlapping of the merging fronts. As a simple two-dimensional example, consider Figure 3.1.

The vertices $V_1$ and $V_2$ are the starting points. If these vertices are simply projected onto the blank plane then the "unforming" of the remaining vertices will lead to possible overlapping. In a extreme case vertices ***b*** and ***c*** would switch positions.

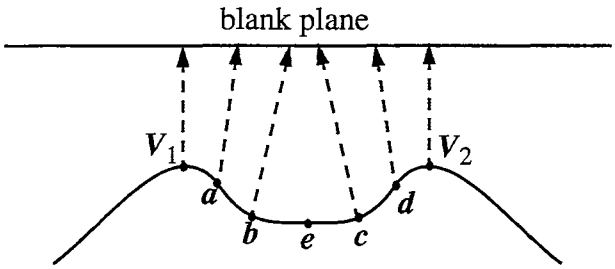


**Figure 3.1 Two-dimensional example of the overlapping of two merging fronts.**

After analyzing the figure, one can conclude that the simple projection of the starting points on the blank plane is not sufficient and that each developing front needs to have some kind of information about other developing fronts and their positions.

## 3.2 Peak Information and Connection

The idea behind this method is to recognize the influential peaks on the surface and connect them in a graph. Peaks are sorted in terms of influence according to specific criteria, namely:

- Height of the peak above a certain mean Z-value of the surface.
- Curvature of the peak.
- Distance from other peaks.

Surfaces are cataloged depending on the number of peaks. The peaks can either be:

- Major peaks: peaks with largest Z-value within some tolerances.
- Minor peaks: peaks that meet the criteria in terms of curvature but have a lower Z-value than major peaks.

Given this categorization, two distinct situations can occur:

1.The surface has one major peak and several or no minor peaks. In this category are included the surfaces studied by Nair.

2.The surface has two or more major peaks and several or no minor peaks.

These situations were investigated separately as follows in the next sections. For each situation, the peaks taken into account were selected interactively.

### 3.2.1 One Major Peak

When only the major peak is selected, then that peak is taken has the starting point and the mapping algorithm is similar to Nair's formulation. However if, in addition to the major peak, other minor peaks are selected the following procedure is applied:

1.Nair's algorithm is used to obtain a preliminary blank shape using the major peak as the starting point. The blank XY coordinates of all the minor peaks are noted.

2.According to the influence of each minor peak, its XY coordinates on the final blank plane are found by weighed interpolation between its position in the preliminary blank shape and the position obtained by simply projecting the minor peak directly onto the blank plane (see Figure 3.2). The weight is calculated according to a normalized peak's influence. This influence is calculated by taking into account

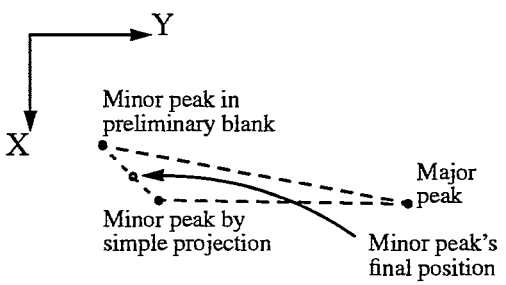


**Figure 3.2 Interpolation to find final blank position of minor peaks**

each minor peak's height above the mean Z-value plane of the surface and its curvature. The two factors are added and normalized against the major peak to which a normalized weight of 1.0 is assigned. The more influence, the closer the final position is to the simply projected position. If the peak does not have any influence in the natural flow of the material then its position will be the one found in the preliminary blank using Nair's formulation. The final weight also includes a normalized factor specified by the user that determines either full influence (factor equals 1) or no influence (factor equals zero) or anywhere in between.

3. The shortest path from the major peak to each minor peak is found on the three-dimensional shape. The vertices on each path must also be interpolated in the same manner as the minor peaks. For each vertex in the path, the final XY position on the blank plane is found by interpolating the vertex obtained in the blank in step 1. and the XY position obtained by simply projecting the vertex onto the blank plane.

4. Instead of having a starting point to initialize the algorithm, there is a topological graph of vertices mapped or constrained at the starting time. Nair's formulation is then applied to calculate the remaining points concentrically from the major peak taking into account that some vertices are already mapped.

### 3.2.2 Two or More Major Peaks

The only difference between the method applied to this situation and the one from the previous section is that in step 1, the starting point for the algorithm is the vertex closest to the centroid, in terms of XY coordinates, of the major peaks. The other steps are the same as in the previous section treating the major peaks as minor peaks for the weight calculation and the vertex closest to the centroid as the major peak.

This technique of connecting and constraining the peaks and the vertices in the paths between them proved to be somewhat inadequate since it only allows small weights to be used (user factor of 0.3 or less) and also in the sense that there is no gradual change between con-

strained vertices to unconstrained ones but a rather sudden one where constrained vertices' neighbors are totally unconstrained. This change introduces unbalances in the computation that are compounded as the mapped front extends.

## 3.3 Attraction and Repulsion Between Peaks

After analyzing the results from the two previous sections, some conclusions can be drawn:

- There should be only one developing front. More than one front leads to problems at the merging points due to the opposite flows of material.
- There should be a priori information of positioning of influential peaks.
- Each peak has a "zone" of influence where vertices in this area can possibly be constrained in their position. These constrained vertices are not limited to the ones lying on the path between two peaks.

These considerations led to a different approach. One can think of each pair of peaks as a sort of "magnets" possessing a mutually repulsive force. In this approach, each peak tries to influence the flow of material outwards from the interior. When a vertex is in one or more zones of influence, then the resulting position will depend on the resultant of all the "forces" acting on it. The flow of material within the zone of influence will tend to be move perpendicularly from the line connecting the peaks (see Figure 3.3.)

This method proved to be more successful than the previous one. However, vertex location will depend not only on area considerations but also on the influence of the peaks.

The concern that the area conservation will be lost needs to be addressed. The conservation of area of every triangular element does not provide enough flexibility for dealing with this multiple peak method. Due to the presence of very influential peaks in the flow of material there might be some large shearing involved resulting in area changes for some triangular

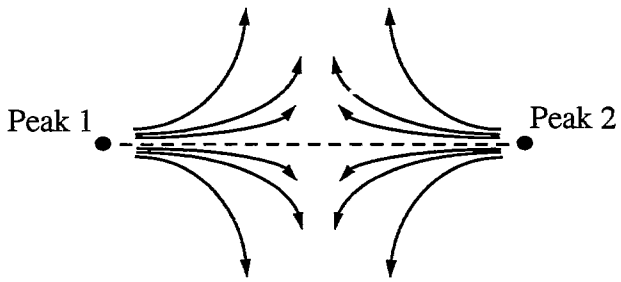


**Figure 3.3 Flow of material within the zone of influence of two peaks.**

entities. For this reason an alternative method that still preserves the overall area was developed and employed to surfaces with more than one major peak. The next chapter introduces this method and shows the results obtained for some example surfaces.

# 4. ALTERNATIVE MAPPING STRATEGY

## 4.1 General Description

The development of this new strategy evolved from the concepts dealing with the mapping of surfaces with several peaks presented in the previous chapter. As mentioned in the previous chapter the handling of complex surfaces with multiple peaks requires a mapping strategy that allows the flexibility to move the mapped vertex without losing, to a certain degree, the conservation of area in relation to its neighbors. This has triggered the idea of mapping the vertex preserving the area of the quadrilateral formed by the vertex in question and the three mapped neighbors, as opposed to preserving the area of each individual triangle (see Figure 4.1.)

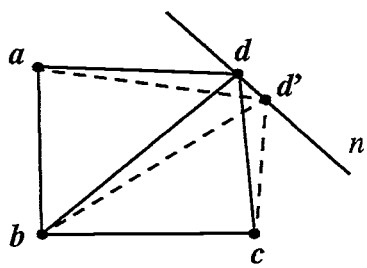


**Figure 4.1 Mapping principle for conserving the area of the quadrilateral.**

As shown in Figure 4.1, the position of a vertex can be defined in a locus line that preserves the total area of the quadrilateral. Given the three mapped vertices ***a***, ***b*** and ***c***, the vertex to be mapped is originally placed at ***d*** by using Nair's area preserving technique. The vertex can however be moved to position ***d'***, based on a constrainment criteria determined by the influence of a given peak, without changing the area of the quadrilateral formed by the verti-

ces ***a***, ***b***, ***c*** and ***d***. Since the area of each quadrilateral is preserved, the total area of the surface is also preserved and so the assumption of an ideal process with no change in thickness (plane strain) is still true.

## 4.2 Application to Multi-Peak Mapping

This mapping strategy can now be applied in conjunction with the method described in Section 3.3 for mapping surfaces with multiple peaks. At this point however, before this method is described in more detail, a few concepts referred to in the last Chapter, need to be more clearly defined.

For the remainder of this chapter, the term "constrained vertices" refers to vertices whose mapped position is found by 1) calculating a preliminary position using a constant area transformation and 2) modifying that position using the method described in Section 4.1 to take into account possible multiple peak influence. "Zone" of influence of two peaks is a region calculated on the blank where vertices which lie inside this region will be constrained or modified from their original position. The procedure used to find these areas will be described later in the chapter.

When two peaks are constraining, the flow of material will be outwards from the line connecting the peaks. This is equivalent to assuming that when the forming operation occurs, the material necessary to fill in the cavity between the peaks flows in primarily from a direction perpendicular to the connecting line between them, and not so much from sliding of material over the peaks.

The influence created by the peaks has a dipolar characteristic, i. e., only when two peaks are present will there be some sort of influence on a given vertex. The factors involved in the calculation of the amount of influence exerted on that vertex are the following:

- Differences in the areas of each triangle formed by two mapped vertices and the vertex in question as in Nair's constant area transformation (see section 2.3.)
- The perpendicular distance from the vertex to the line connecting the two peaks.
- The distance of the from each peak.

The reasoning behind the use of these factors follows from the considerations stated in Chapter 3. Vertices that are closer to the line connecting the two peaks are less influenced than vertices that are offset from the connecting line due to the dipolar characteristics, and vertices that lie on the connecting line will not be constrained at all except to the usual area constrainment. Also the influence will be strongest at a distance half way from each peak. By observing Figure 4.2 one can notice that vertex ***c*** will be less affected than vertex ***a*** since it is closer to the line connecting the peaks (the vectors applied at ***a*** and ***c*** represent the repulsive forces exerted by each peak. One can see that the resultant force will be larger at ***a*** than at ***c***.) Also

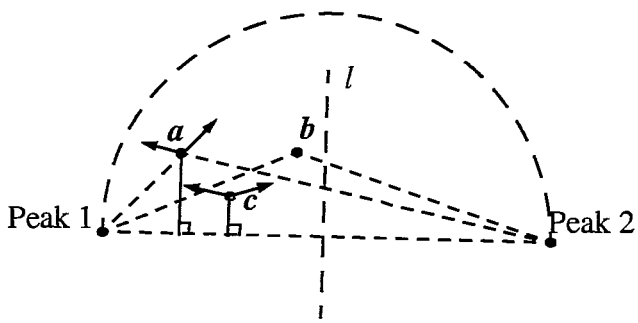


**Figure 4.2 Influence of peaks on the positioning of vertices within the area of influence.**

vertex ***b*** is more influenced than vertex ***a*** due to its position closer to the middle line *l*. The semi-circumferential line connecting the peaks shown in the figure is a boundary line that determines which vertices will be under the influence of the peaks. The following heuristic mapping algorithm was formulated according to these assumptions.

Distances between mapped vertices and peaks are taken as the XY distances between the already mapped vertices via constant area transformation and the projections of the peaks onto the blank plane. The steps involved in the positioning of constrained vertices are as follows:

1. Given a vertex $V$ calculate the mapped position $V'$ of the vertex $V$ according to the unconstrained constant area transformation (Section 2.3).

2. Determine which are the two closest peaks to $V'$. Determine if $V'$ is inside the area of influence of these peaks (see Figure 4.2.) If so, then the peaks are labeled $P_1$ and $P_2$ and the vertex $V'$ needs to be additionally constrained. If the vertex $V'$ does not lie inside the zone of influence then repeat step 2 using the second and third closest peaks. Do this until the vertex is determined to be constrained or if the vertex cannot be influenced by any two peaks then it is unconstrained and $V'$ is its final position.

3. If the vertex $V'$ is determined to be constrained according to step 2, then four position modifying factors are computed:

   - Area factor. This factor takes into account large area differences in adjacent triangles that can result from large shearing. It is determined based on the area differences of the two triangles used for the constant area transformation (see Section 2.3.) Given the triangular areas $A_1$ and $A_2$, the area factor is:

$$k_a = 1 - A_1/A_2 \qquad \text{for } A_1 < A_2$$

$$k_a = 1 - A_2/A_1 \qquad \text{for } A_1 > A_2$$

   - Distance factor. This factor takes into account the perpendicular distance from the line connecting the two peaks. It is computed using the angle described between the lines connecting vertex $V$ and the two peaks. From figure 4.2 one can see that if this angle is greater than 90 degrees then the vertex lies outside the zone of influence. Given an angle $\theta$, the distance factor is:

$k_d = 1 - 1/2\ (\theta/90)$

- Center factor. This factor depends on the distance of the vertex $V$ from the center line dividing the two peaks (line $l$ in figure 4.2.) Given the distances $d_1$ and $d_2$ defined from $V$ to $P_1$ and $P_2$, the center factor is defined as:

$$k_c = 1/2\ (1 + d_1/d_2) \qquad \text{for } d_1 < d_2$$

$$k_c = 1/2\ (1 + d_2/d_1) \qquad \text{for } d_1 > d_2$$

- Projection factor. It is determined based on the projection of the resulting "force" vector onto the locus line that defines the a constant area quadrilateral (see Figure 4.3). Given two vectors $\boldsymbol{u}_1 = \boldsymbol{V} - \boldsymbol{P}_1$ and $\boldsymbol{u}_2 = \boldsymbol{V} - \boldsymbol{P}_2$, the resultant vector $\boldsymbol{u} = \boldsymbol{u}_1 + \boldsymbol{u}_2$ and the projection $\boldsymbol{u}_p$ onto the locus line $n$ as defined in Figure 4.3, then the projection factor is defined as:

$$k_p = |\boldsymbol{u}_p| / |\boldsymbol{u}|$$

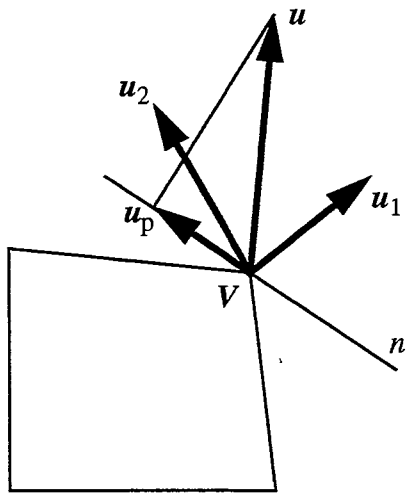


**Figure 4.3 Calculation of the projection factor.**

4. The overall correction factor for the repositioning of $V'$ is obtained by multiplying all the factors defined in step 3. The new position of $V'$ is calculated by applying the correction factor to the preliminary mapped vertex along the locus line of conservation of the quadrilateral area $n$.

$$k = k_a k_d k_c k_p$$

$$V'_{\text{corrected}} = V' + k\, \boldsymbol{u}_p / |\boldsymbol{u}_p|$$

The algorithm is initialized in the same manner as described in section 3.2. Depending on the number of major peaks, the starting point will be either a major peak in the case there is only one present, or the vertex closest to the centroidal XY position of all the major peaks.

## 4.3 Mapping Examples

This modified multi-peak constant area transformation algorithm was applied to two example surfaces and the results are compared to the ones obtained using Nair's original formulation.

### 4.3.1 Surface With Two Peaks

Figure 4.4 represents a non-uniform rational B-spline surface with two major peaks. This surface was used as an example to illustrate the differences between Nair's constant area formulation and the multi-peak formulation presented above. In the multi-peak method only

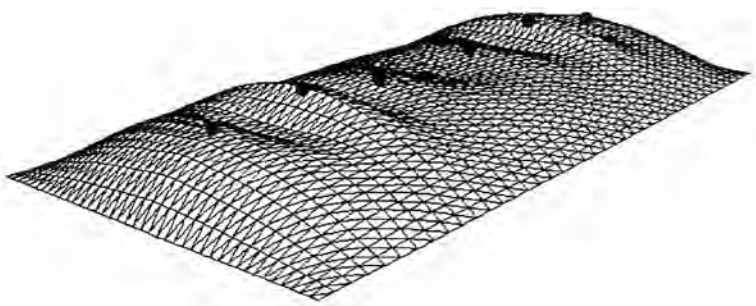

**Figure 4.4 NURBS surface with two major peaks.**

the two major peaks were selected. The minor peaks that are also present are of small influence and therefore were not accounted for. The starting point for Nair's algorithm is selected as either one of the two major peaks. Using Nair's algorithm, selection of either starting point will result in some non-symmetries despite the fact that the original surface is symmetric. The resulting blank is shown in Figure 4.5.

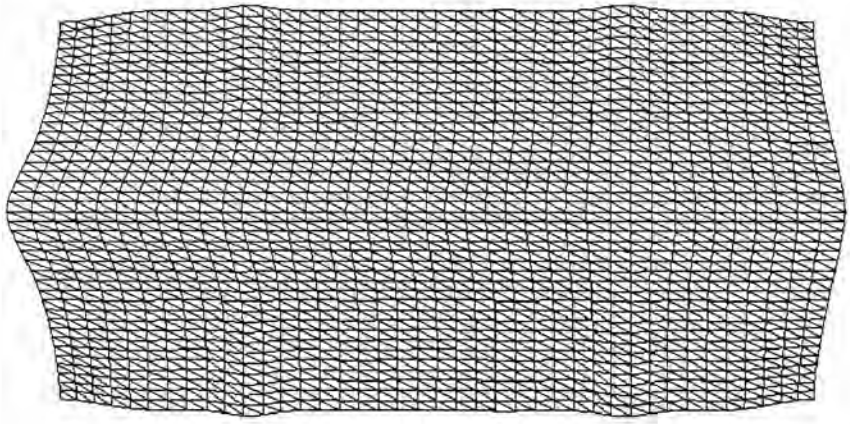

**Figure 4.5 Developed blank using Nair's constant area transformation.**

Using the new algorithm applied to the surface in Figure 4.4, the starting point will be the vertex closest to the centroid of the two major peaks projected onto the blank plane. This ensures that symmetry is preserved. The flow of material is constrained by the two peaks. Figure 4.6 shows the resultant blank. When comparing this result to Figure 4.5, it is observed that there is more flow of material towards the top and bottom. This is in agreement with the assumptions made about the effects of multiple peaks.

### 4.3.2 Surface With Multiple Minor Peaks

The following example was chosen to illustrate how the multi-peak algorithm can be applied to more complex surfaces. Figure 4.7 shows a NURBS surface with one major peak and several minor peaks. This surface has been previously studied by Nair [20] but due to its complex shape, it is the belief of the author that the simple constant area transformation is not

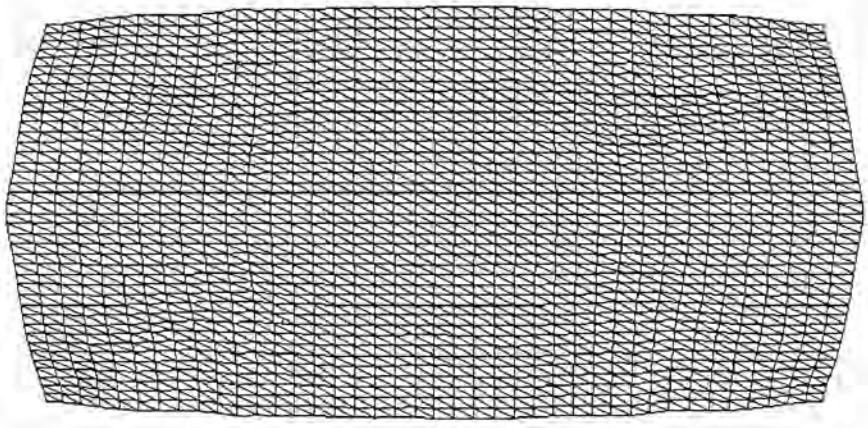

**Figure 4.6 Developed blank using the multi-peak algorithm accounting for the two major peaks.**

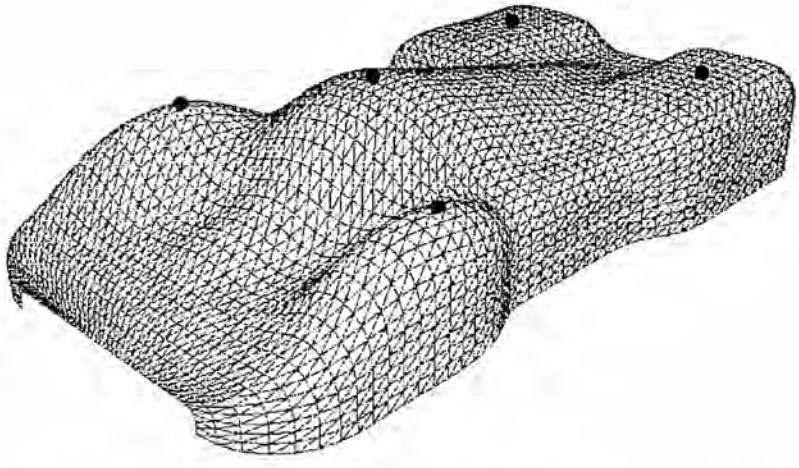

**Figure 4.7 NURBS surface with several minor peaks.**

realistic enough in terms of results. The developed blank obtained by Nair is shown in Figure 4.8.

One can see in Figure 4.8 that, although the constant area formulation handles this complex shape reasonably well, there are a few problematic regions on the left hand side. This region corresponds to the front of the car model and apparently induces high strains where

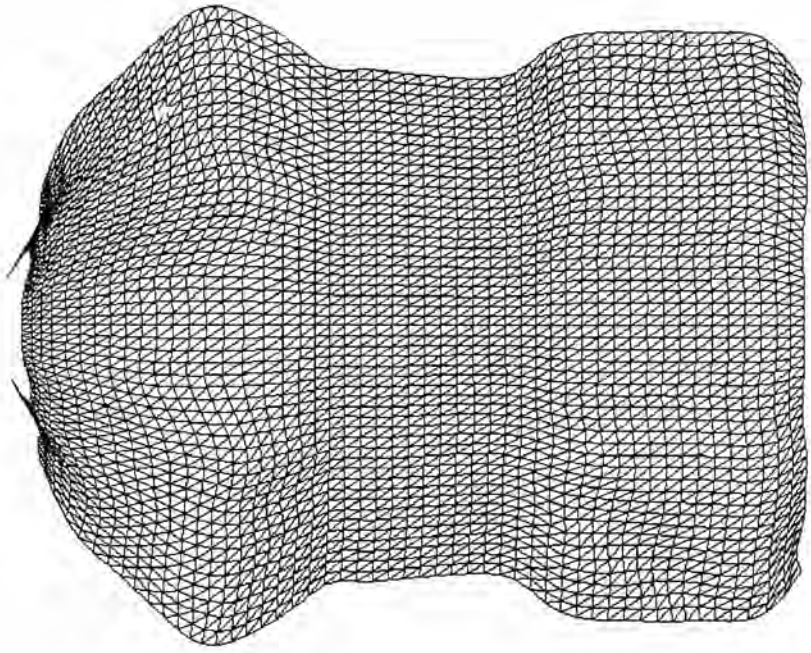

**Figure 4.8 Developed blank using Nair's constant are formulation.**

large shear could occur. If the geometry of the two front peaks is taken into account (see Figure 4.7) and also if friction is present, those regions might create even more problems.

The same surface was then used as the input for the multi-peak algorithm. Five peaks were selected. The major peak in the center, the two peaks over the front wheels and two peaks over the rear wheels. The resulting blank can be seen in Figure 4.9.

As predicted the problems encountered previously in the regions of high shear are aggravated using the multi-peak algorithm. The wrinkling that occurs in those areas can give an indication that the given design surface of Figure 4.7 cannot be manufactured by press forming only. The designer may then redesign the surface to account for these problems. However, the rear bumps on the surface do not seem to present many problems.

The multi-peak method presented in this chapter proved to be more successful when dealing with complex surfaces than previous ones. It is the opinion of the author, however,

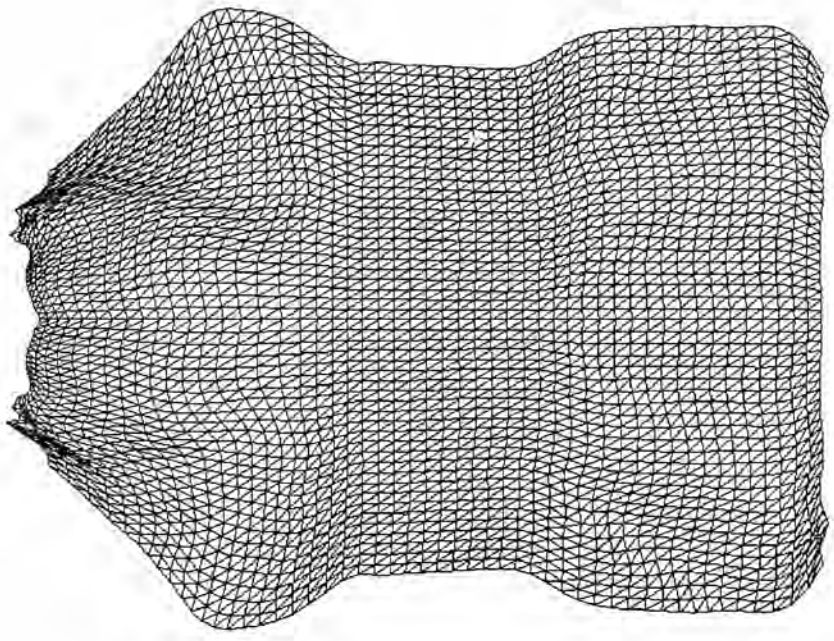

**Figure 4.9 Calculated blank using the multi-peak algorithm.**

that the limiting factor in this studies, more than the conservation of triangular area as presented by Nair, is the assumption of an ideal process without any thickness change. These concerns were addressed during the course of this research and some of the observations and results are presented in Chapter 6.

# 5. GEOMETRIC SURFACE STRAINS

This chapter presents a method of determining the geometric surface strains which can be used with both Nair's constant area transformation or the algorithms presented in this thesis to provide additional information about the formability of a given surface as well as validate the results obtained by the blank development algorithms presented. The theory of finite strain based on the homogeneous deformation mode is used to formulate the algorithm.

## 5.1 Strain Theory

The deformation of a rigid body produces a change in its nominal dimensions. These changes can be measured or determined analytically for many cases. Consider a length $l_0$ which under loading changes to $l$ such that $l \neq l_0$. Although, both translation and rotation may occur during the loading process, it is the change in length that is used to define strain as,

$$e = \frac{l - l_0}{l_0} = \frac{\Delta l}{l_0} \tag{5.1}$$

where $e$ is the nominal or engineering strain. For large strains, however, the logarithmic, natural, or true strain $\varepsilon$ is more commonly used. True strain is defined such that every incremental length change is divided by the current length,

$$d\varepsilon = \frac{dl}{l} \tag{5.2}$$

which after integrating gives,

$$\varepsilon = \ln\frac{l}{l_0} \tag{5.3}$$

True strains are more convenient than engineering strains because:

1.True strains for equivalent deformation in tension and compression are identical except in sign.

2.True strains are additive, the total strain being the sum of the incremental strains. This is not true for engineering strains.

3.The volume change is related to the sum of the three normal strains, and the volume conservation relationship is given by,

$$\varepsilon_x + \varepsilon_y + \varepsilon_z = 0 \tag{5.4}$$

4.If the strains are small, then true and engineering strains are nearly equal.

Expressing equation (5.3) as,

$$\varepsilon = \ln\left(\frac{l_0 + \Delta l}{l_0}\right) = \ln\left(1 + \frac{\Delta l}{l_0}\right) = \ln(1 + e) \tag{5.5}$$

a series expansion results in

$$\varepsilon = e - \frac{e^2}{2} + \frac{e^3}{3!} + \ldots\ldots \tag{5.6}$$

as $e \to 0, \varepsilon \to e$ [24].

## 5.2 Finite Strain

In forming metals, deformations may be large and the instantaneous strength of any material element varies during the process. The strain itself is a function of the deformation

history. In sheet metal forming, strain measurements are often made by marking a grid on the surface. If the grid is measured after a small increment in deformation, the strain increment is, in general, easily determined. The mode of deformation will dictate how readily the strain increment in each successive deformation step can be evaluated from the distorted grid, and how easily the strain increments can be integrated. In many instances, however, it is either too time consuming or difficult to make incremental measures and only measurements of the initial and final shape of the grid are made.

## 5.3 Circular Grid Analysis

Largely by convention, in sheet metal stamping it is assumed that one principal axis of plastic strain increment is normal to the material surface, with the other two principal directions lying in the plane of the sheet. The well known circular-grid analysis technique [26] for determining strains in sheet metal pressings is based on this hypothesis. The method also assumes that a grid circle, etched or printed on an un-deformed blank, is transformed into an ellipse on the surface of the pressing.

By measuring the major and minor diameter of the ellipse, the principal surface strains are determined. Although over a large portion of the surface, circles transform into approximate ellipses, not every element deforms in this manner. In general, the deformation path of an element in an industrial pressing is not known precisely. The degree to which the measurements of a grid circle reflect the actual strain is a matter of conjecture and actually depends upon the complexity of the strain path. In the presence of high strain gradients the grid circle method is inadequate, since a grid circle will undergo severe distortion and no longer resembles an ellipse after deformation. The grid circle analysis technique however, reduces the strain determination to a two dimensional problem since the deformed ellipse lies on a relatively flat surface.

Another major limitation of the circular grid analysis procedure is the physical limit of the circle size due to the equipment capability for etching or printing the circle on the blank. Ideally, if the circles are small enough, then even in the areas of high strain gradients, the grid circles will undergo only plane strain along the principal directions.

If this technique is used incrementally it will indicate whether the principal strain ratios are in constant proportion, however it will not demonstrate whether the principal axes remain fixed with respect to the material element. This is because rotation of the major and minor axes around the deformed circle cannot be determined.

## 5.4 Homogeneous Deformation

The deformation process which transforms straight lines into straight lines and circles into ellipses is usually referred to as homogenous deformation [25]. As the region is deforming in a pure homogeneous mode, the element remains orthogonal and principal directions remain fixed with respect to the material element. This is exemplified by the pure shear mode. Only the principal axes remain fixed in direction, all other line elements rotate. It is well known that the final shape of a material element following a prescribed homogenous strain, can also be realized by imposing a pure homogenous mode followed by a rigid body rotation. This poses the question of equivalence of the strain paths. Sowerby et al. show that the pure homogenous deformation mode leads to a simple finite strain tensor, analogous to the infinitesimal strain tensor but without the need to introduce any simplifying assumptions [27].

Sowerby's method eliminates some of the problems encountered in strain calculations using the circular grid analysis [27]. Specifically, the uncertainty of assessing the major and minor axis of an ellipse is eliminated, and an improved averaging of the strain within an element becomes available. Emphasis is placed on the pure homogenous mode, since it leads to a simpler finite strain tensor. Marciniak and Duncan also introduce a nodal strain analysis very

similar to Sowerby's in which a pure homogeneous mode of deformation is considered [28]. The strain distribution is determined from the initial and final configuration of an array of points on the surface.

## 5.5 Two Dimensional Homogeneous Strain

The method presented applies in two dimensions only and is based on Marciniak's studies in experimental strain analysis [28] and Sowerby's analytical method [27]. In sheet metal forming, the third principal stress is generally perpendicular to the surface of the sheet and strain is determined from grid markings made on the surface so that the two-dimensional description will apply.

As shown in Figure 5.1, the initial grid defines locally an orthogonal set of axes $OX_1$, $OX_2$ in which the unknown principal axes, 1, 2, are oriented at an angle θ. A general point

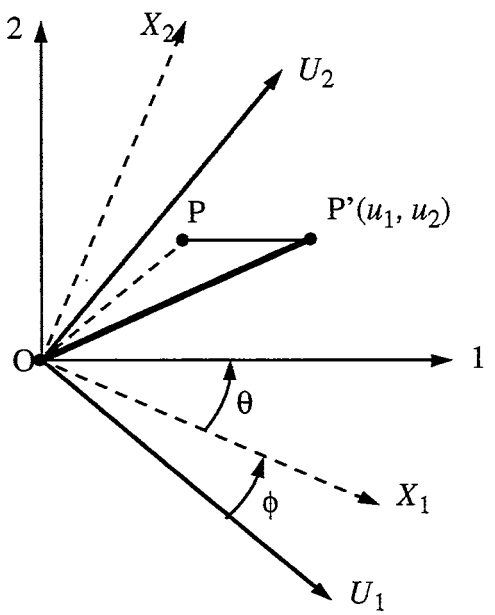


**Figure 5.1 Displacement PP' of a point in the grid axes and in the measuring axes [28].**

P($x_1$, $x_2$), after deformation will have some position P' which is measured in the frame defined by an arbitrary set of measuring axes $OU_1$, $OU_2$. The angle $\phi$ between the measuring axes and the grid axes is not known because any grid marks on the material initially along the $OX_1$ and $OX_2$ axes will have rotated with deformation. If the initial array consists of the points DAB in Figure 5.2(a), the problem is to find the principal elongations $e_1$ and $e_2$ and the orientation $\theta$ of

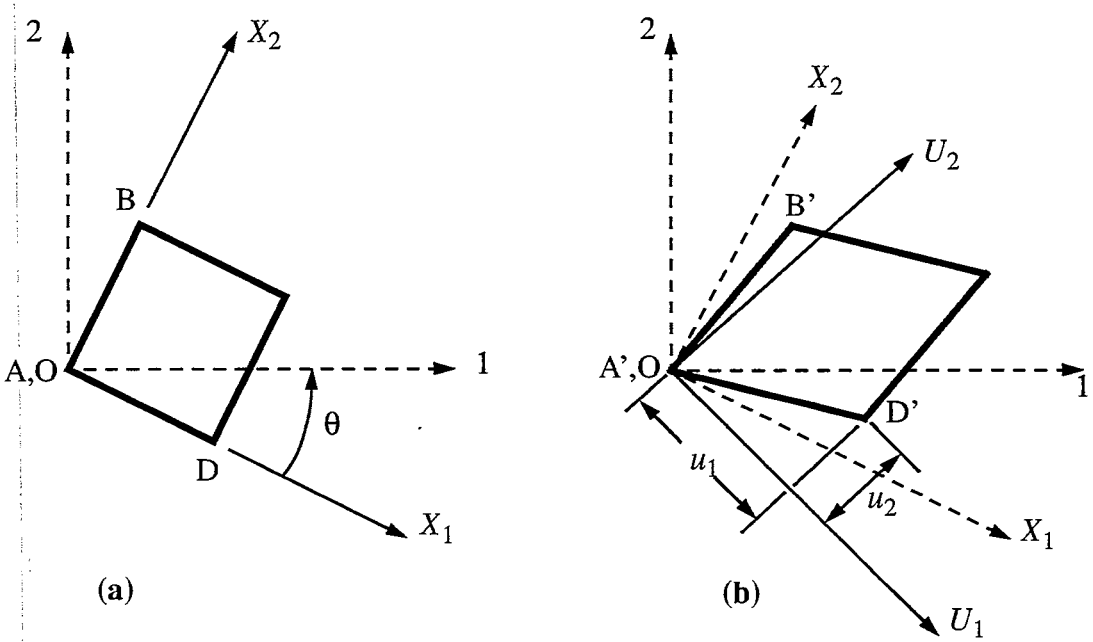


**Figure 5.2 (a) Initial square grid in the undeformed sheet; (b) deformed points B' and D' in the arbitrary measuring axes $OU_1$, $OU_2$ [28].**

the principal directions in terms of the coordinates $u_1$ and $u_2$ of the deformed array in the arbitrary measuring axes as seen in Figure 5.2(b). The solution is more easily expressed in tensor notation.

The coordinates ($u_1$, $u_2$) of a vertex can be expressed as a linear function of its coordinates in the unformed state ($x_1$, $x_2$) as

$$\begin{aligned} u_1 &= F_{11}x_1 + F_{12}x_2 \\ u_2 &= F_{21}x_1 + F_{22}x_2 \\ \bar{u} &= \underline{F} \cdot \bar{x} \end{aligned} \tag{5.7}$$

or

$$\begin{Bmatrix} u_1 \\ u_2 \end{Bmatrix} = \begin{bmatrix} F_{11} & F_{12} \\ F_{21} & F_{22} \end{bmatrix} \begin{Bmatrix} x_1 \\ x_2 \end{Bmatrix} \tag{5.8}$$

where the coefficients of (5.8) represent the displacements of the initial point to the final configuration. These coefficients can be determined with reference to Figure 5.2 using,

$$\begin{aligned} u_1(B') &= F_{11}x_1(B') + F_{12}x_2(B') \\ u_2(B') &= F_{21}x_1(B') + F_{22}x_2(B') \\ u_1(D') &= F_{11}x_1(D') + F_{12}x_2(D') \\ u_2(D') &= F_{21}x_1(D') + F_{22}x_2(D') \end{aligned} \tag{5.9}$$

or, using matrix form,

$$\begin{Bmatrix} u_1(B') \\ u_1(D') \\ u_2(B') \\ u_2(D') \end{Bmatrix} = \begin{bmatrix} x_1(B') & x_2(B') & 0 & 0 \\ x_1(D') & x_2(D') & 0 & 0 \\ 0 & 0 & x_1(B') & x_2(B') \\ 0 & 0 & x_1(D') & x_2(D') \end{bmatrix} \begin{Bmatrix} F_{11} \\ F_{12} \\ F_{21} \\ F_{22} \end{Bmatrix} \tag{5.10}$$

By inverting this matrix the four coefficients can be determined as,

$$\begin{Bmatrix} F_{11} \\ F_{12} \\ F_{21} \\ F_{22} \end{Bmatrix} = Det \begin{bmatrix} x_2(D') & -x_2(B') & 0 & 0 \\ -x_1(D') & x_1(B') & 0 & 0 \\ 0 & 0 & x_2(D') & -x_2(B') \\ 0 & 0 & -x_1(D') & x_1(B') \end{bmatrix} \begin{Bmatrix} u_1(B') \\ u_1(D') \\ u_2(B') \\ u_2(D') \end{Bmatrix} \tag{5.11}$$

where $Det = \dfrac{1}{x_1(B')x_2(D') - x_1(D')x_2(B')}$

The coefficients $F_{11}, F_{12}, F_{21}$ and $F_{22}$ can be combined in such a way that they always yield the same components of a symmetric second order tensor, $\underset{\sim}{C}$, known as Green's deformation tensor such that,

$$\underset{\sim}{C} = \underset{\sim}{F}^T \cdot \underset{\sim}{F} \tag{5.12}$$

Expanding the above equation, the components of the symmetric tensor are,

$$\begin{aligned} b_{11} &= F_{11}^{\,2} + F_{21}^{\,2} \\ b_{12} &= b_{21} = F_{11}F_{12} + F_{21}F_{22} \\ b_{22} &= F_{12}^{\,2} + F_{22}^{\,2} \end{aligned} \tag{5.13}$$

Notice that if the initial square DAB in Figure 5.2 is a unit square then equation (5.13) reduces to,

$$\begin{aligned} b_{11} &= u_1(D')^2 + u_2(D')^2 \\ b_{12} &= b_{21} = u_1(D')u_1(B') + u_2(D')u_2(B') \\ b_{22} &= u_1(B')^2 + u_2(B')^2 \end{aligned} \tag{5.14}$$

which is the form used by Marciniak [28]. The principal values are then given by,

$$\left(1+e_{1,2}\right)^2 = \frac{\left(b_{11}+b_{22}\right)}{2} \pm \sqrt{\left(\frac{b_{11}-b_{22}}{2}\right)^2 + b_{12}^2} \tag{5.15}$$

and the orientation is determined according to,

$$\tan 2\theta = \frac{2b_{12}}{b_{11}-b_{22}} \tag{5.16}$$

The logarithmic strains are found using,

$$\varepsilon_1, \varepsilon_2 = \ln\left(1+e_1, e_2\right) \tag{5.17}$$

This strain calculation procedure was implemented and applied to the constant area algorithms previously discussed. See the details in the Appendix on page 49. The results for two examples surfaces used previously are shown in the next section.

## 5.6 Discussion

The strains are displayed as color coded images for emphasis and ease of interpretation. Strains were colored in the standard color spectrum range between violet and red signifying pure tension and compression respectively.

The geometric strain algorithm was applied to the surface of Figure 4.4 assuming there was no thickness change throughout the forming process. The two major peaks were selected and the multi-peak algorithm described in Chapter 4 was used to calculate the blank. The computed major and minor strains are shown in Figure 5.3. The strain analysis shows a rather uniform spread of surface strains with the largest shear occurring closer to the corners.

The second example surface is the one from Figure 4.7. For this example, only the major peak was selected ignoring the influences of the minor peaks. The resulting strain distribution is shown in Figure 5.4. As expected, the areas of larger strain are the regions in the

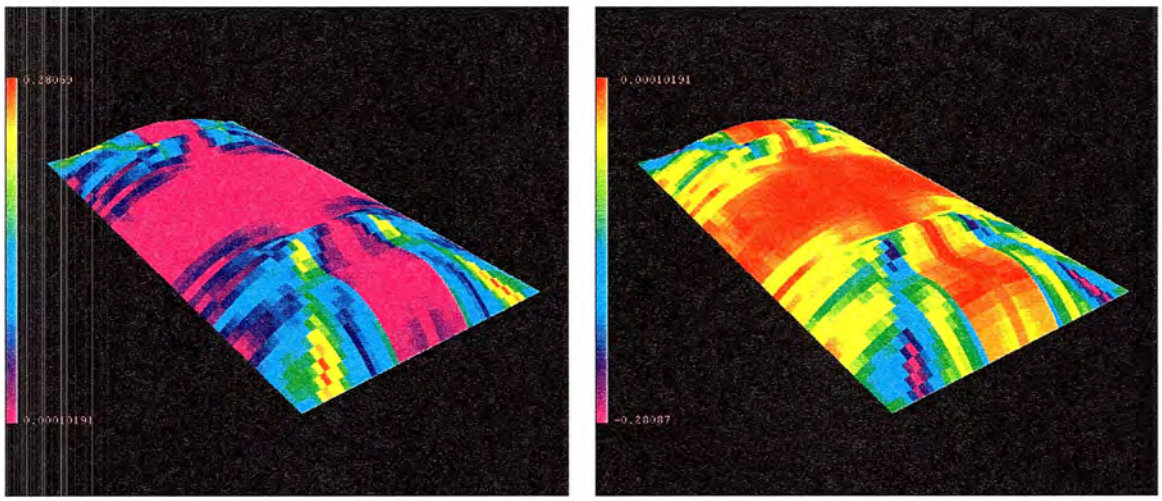

(a) (b)

**Figure 5.3 Surface with two peaks. (a) Major strain. (b) Minor strain.**

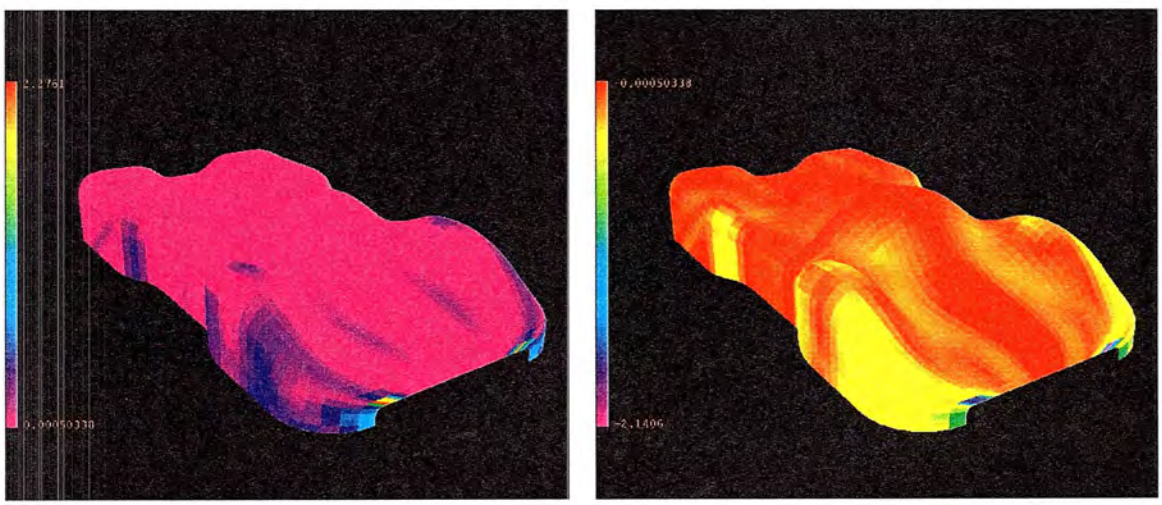

(a) (b)

**Figure 5.4 Surface with multiple peaks. (a) Major strain. (b) Minor strain.**

front, implying that fracture might occur at those points during forming. These results agree with the observations made in Chapter 4 for the same surface.

If the major strain is plotted against the minor strain the points fall on a straight line with a slope of minus 45 degrees. This validates the assumption of pure shear and of the constancy of area throughout the surface. The information provided by the strain analysis can also be useful for the designer to locate potential fracture regions in the piece. As the constant area algorithm, the geometric strain algorithm is computationally inexpensive and suitable for interactive use.

# 6. VOLUME CONSERVATION MAPPING

The analysis of the constant area mapping algorithm for multiple peaks indicates that the assumption of an ideal forming operation without thinning is too restrictive and not very realistic in some cases. The volume conservation mapping procedure is an attempt to generalize the mapping to take into account possible thickness changes in the part during forming.

The method developed in this research is based on the constant area transformation algorithm developed by Nair [20] and briefly discussed in Chapter 2. Nair assumes an ideal process, in which there is no thinning and therefore the volume of material contained within any triangle remains constant throughout the forming process. Nair's algorithm transforms the formed three dimensional geometry into an initial planar shape.

## 6.1 General Considerations

The constant volume algorithm can be considered as an extension of Nair's formulation. Here the thickness is allowed to vary at each point and the unformed shape of the blank is calculated on the basis of a constancy of volume. The algorithm has linear time complexity, an attractive feature also present in Nair's algorithm. The constant volume transformation algorithm, however, produces more realistic results since it does not assume a state of plane strain, i.e., no change in thickness during the process.

In addition to the formed surface geometry in polygonal form, this method requires specification of a thickness distribution which is generally not constant. With only the geometric information, the design engineer can predict variations in thickness on the final

(formed) piece and use those predictions as input to the algorithm or, if there is a prototype part available, it could be measured and used as input.

This algorithm was only applied to simple geometrical shapes with one starting point. The techniques discussed in Chapter 3 and 4 on multiple peak method were not implemented with this algorithm.

Some of the basic assumptions found in Nair's algorithm are also used here, such as:

- The initial surface is represented by a grid of points (vertices) which are considered as the elementary surface entities.
- The surface is continuous, homogeneous and isotropic.
- Only plastic deformation is considered.

The new assumptions underlying the constant volume mapping algorithm are as follows:

- The formed shape is defined by two surfaces. The initial design (upper) surface characterizes the geometrical shape. The second (lower) surface has the same number of vertices as the upper surface which are projected from the original ones along the normal vectors relative to the design surface, producing a formed shape with a defined thickness at each point.
- Elemental volume entities (triangular prisms) are formed from any three adjacent non-colinear vertices of the upper surface and the topologically corresponding (i.e., same *i*th and *j*th values) three vertices of the lower surface.
- At the final or undeformed state of the algorithm the vertices on the upper surface will have the same X and Y coordinates as the ones on the lower surface. The Z-coordinate of the vertices on the lower surface will be offset from the Z-value of the corresponding vertex on the upper surface by a certain average thickness value. This average thickness is calculated as an average of the initial thickness distribution of the part.

## 6.2 Volume Geometry Representation

### 6.2.1 Design (upper) surface

The upper surface may be represented using a non-uniform rational B-spline (NURBS) surface. This surface is represented as

$$s(u,v) = \sum_{i=0}^{m}\sum_{j=0}^{n} \boldsymbol{P}_{i,j} N_{i,k}(u) N_{j,l}(v) \qquad u, v \in [0,1] \tag{6.1}$$

where $\boldsymbol{S}(u,v)$ is a three dimensional vector function of control points $\boldsymbol{P}_{i,j}$ arranged in a topologically rectangular grid and $N_{i,k}(u)$ and $N_{j,l}(v)$ are the degree $k$ and $l$ B-spline basis functions, respectively [29].

The surface is approximated by a faceted polyhedron composed of a ($M$ x $N$) set of three dimensional vertices $\boldsymbol{V}_{ij} = \boldsymbol{S}(u_i,v_j)$, $i = 1,...,M$ and $j = 1,...,N$. In this application, the surface is triangulated in uniform parametric intervals to form a topologically rectangular mesh, which, after mapping through $\boldsymbol{S}(u,v)$ generates a uniform network. In the topology created, each internal vertex has eight surrounding vertices as shown in Figure 6.1.

The topological information is stored independently of the geometric information, a useful advantage of the parametric surface representation. Any surface vertex in Euclidean

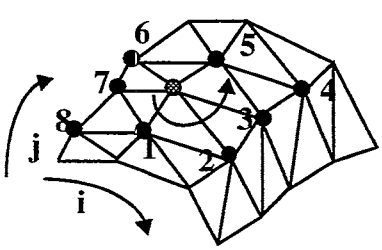


**Figure 6.1 Discretized surface model with vertex adjacency relationships and numbering system**

space has a dual in the parametric space [20]. The topology of the surface approximation is defined in the parameter space while the corresponding geometrical information, which is used mostly for area and volume calculations, is defined in Euclidean space.

### 6.2.2 Lower (created) surface

This surface is created using the following procedure:

- the normal vector $\boldsymbol{n}_{ij}$ at each vertex of the design surface is calculated. If the surface input is in the polygonal form, $\boldsymbol{n}_{ij}$ can be computed from neighboring faces.
- a point of the lower surface $\boldsymbol{V}_{ij}$ is calculated by multiplying the corresponding normal vector ($\boldsymbol{n}_{ij}$) by an input thickness amount (predicted or based on some previous information).

## 6.3 Algorithm Basis

The following terminology will be used for the remainder of this thesis in order to facilitate the description of the algorithm.

| | |
|---|---|
| $N$ | Total number of vertices on the surface |
| $\boldsymbol{V}^u_{ij}$ | Address and coordinates of a specific vertex on the upper surface, $i$ and $j$ correspond to surface parametric directions $u$ and $v$ |
| $\boldsymbol{V}^l_{ij}$ | Address and coordinates of a specific vertex on the lower surface, $i$ and $j$ correspond to surface parametric directions $u$ and $v$ |
| $\boldsymbol{T}^u_{ij}$ | Address and coordinates of a specific transformed vertex on the upper surface, $i$ and $j$ correspond to surface parametric directions $u$ and $v$ |
| $\boldsymbol{T}^l_{ij}$ | Address and coordinates of a specific transformed vertex on the lower surface, $i$ and $j$ correspond to surface parametric directions $u$ and $v$ |
| $Adj(\boldsymbol{V}_{ij})$ | Vertex adjacency list for each $\boldsymbol{V}_{ij}$ |
| $Flag(\boldsymbol{V}_{ij})$ | 1 - if vertex $\boldsymbol{V}_{ij}$ is transformed, 0 - otherwise |

| | |
|---|---|
| Primary neighbors | Vertices in $Adj(V_{ij})$ which are topologically adjacent to $V_{ij}$ in parameter space, i.e., $V_{i-1j}$, $V_{i+1j}$, $V_{ij-1}$ and $V_{ij+1}$ |
| Secondary neighbors | Other vertices in the $Adj(V_{ij})$ list |

The algorithm uses a basic geometrical shape, a tetrahedron. Three tetrahedra combined form a triangular prism. These prisms form the elemental volume entities in the algorithm (see Figure 6.2).

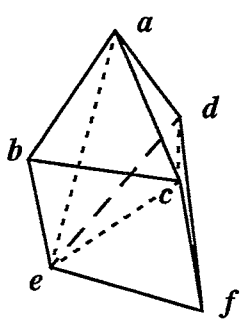


**Figure 6.2 Elemental volume entity**

In Figure 6.2, vertices ***a***, ***b*** and ***c*** belong to the upper surface and ***d***, ***e*** and ***f*** to the lower surface. In the undeformed state (final stage of the algorithm), these vertices define three vertical planes (perpendicular to the XY plane) and two horizontal planes (parallel to the XY plane). Taking this into consideration, the interpretation of the algorithm can be summarized as follows:

- Given the location of four vertices (two adjacent vertices on the top surface and two on the lower surface) that lie on the same vertical plane, a family of triangular prisms with volume V = Vol($V^u_i$, $V^u_j$, $V^u_k$,$V^l_i$) + Vol($V^u_k$, $V^u_j$, $V^l_k$,$V^l_i$) + Vol($V^l_i$, $V^l_j$, $V^l_k$,$V^u_j$) can be defined by the volume locus ***L*** of the points $V^u_k$ and $V^l_k$ which is a plane parallel to the plane ***P*** defined by ($V^u_i$, $V^u_j$, $V^l_i$ and $V^l_j$) at a distance h = 2V/ Area($V^u_i$, $V^u_j$, $V^l_i$,$V^l_j$) from the plane ***P*** (see Figure 6.3.)

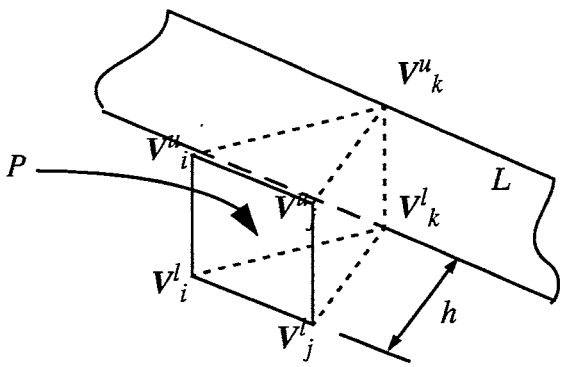


**Figure 6.3 Locus of the third vertices of a family of constant volume prisms or "slices".**

- Given two adjacent prisms $S_1(V^u_i, V^u_j, V^u_l, V^l_i, V^l_j, V^l_l)$ and $S_2(V^u_k, V^u_i, V^u_l, V^l_k, V^l_i, V^l_l)$ in the initial state and corresponding projected locations of any three of the vertices on the upper surface, say $T^u_i$, $T^u_j$ and $T^u_k$ along with the projected locations of the three corresponding vertices on the lower surface, $T^l_i$, $T^l_j$ and $T^l_k$ as shown in Figure 6.4, if the line defined by the unknown common vertices $T^u_l$ and $T^l_l$ is located at the intersection of the volume loci $P_1 \leftarrow S_1$ and $P_2 \leftarrow S_2$, then

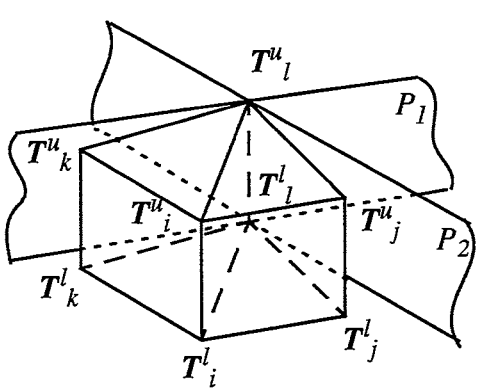


**Figure 6.4 Volume conservation principle.**

$$Volume(V^u_i, V^u_j, V^u_l, V^l_i, V^l_j, V^l_l) = Volume(T^u_i, T^u_j, T^u_l, T^l_i, T^l_j, T^l_l)$$
*and*
$$Volume(V^u_k, V^u_i, V^u_l, V^l_k, V^l_i, V^l_l) = Volume(T^u_k, T^u_i, T^u_l, T^l_k, T^l_i, T^l_l)$$

This represents a generalization of Nair's formulation which used only one surface and the calculations were performed in terms of triangles and area loci. Since it ignored thickness, the problem was one of mapping $E^3$ space to a $E^2$ space. This is not true in this algorithm but the extra degree of freedom is nevertheless constrained by the assumption that the transformed vertices of the lower surface have the same planar coordinates as the corresponding ones on the upper surface. All other characteristics of the algorithm are very similar to Nair's formulation and are described in detail in the following sections.

## 6.4 Transformation Initialization

It is assumed that the point of initial punch contact on the blank is the furthest from the blank plane, an assumption that can be used since we are ignoring friction. Thus the vertex with the largest Z-value is chosen as the starting point of the algorithm. To reverse the forming process, "un-forming" of the surface creates the effect of reversing the flow of material in the actual process. This flow is achieved by allowing the elemental volume entities to transform in a concentric manner starting with the vertices immediately surrounding the starting point as shown in Figure 6.5.

The transformation is initiated by projecting the starting point parallel to the Z-axis, onto the blank plane. The corresponding point on the lower surface is projected along the same vector and is offset from the one on the upper surface by the average thickness calculated from the inputted formed shape as described at the end of Section 6.1. In order to initialize the algorithm the locations of at least four adjacent vertices, two on the upper surface and two on the lower surface. However, a boundary-less deformation implies uniform flow of vol-

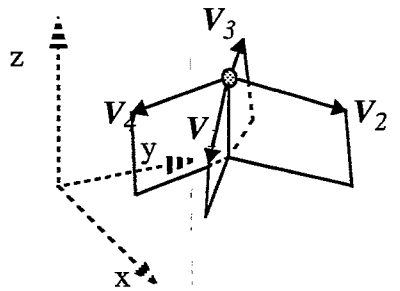


**Figure 6.5 Initial vertex and four primary neighbors.**

ume in all directions. Thus, the locations of all four primary neighbors of the starting point are required. Since volume techniques cannot be used to find the projected locations of these vertices, we apply a vertical area preservation technique to all four primary neighbors of the starting point. This technique consists of the following (see Figure 6.6):

- the XY-direction of the vector $T_1T_0$ is an average of the XY-directions of $V^u{}_1V^u{}_0$ and $V^l{}_1V^l{}_0$
- the length $h$ of the vector $T_1T_0$ is calculated as,

$$h = Area(V^u{}_1, V^u{}_0, V^l{}_1, V^l{}_0) \,/\, AverageThickness$$

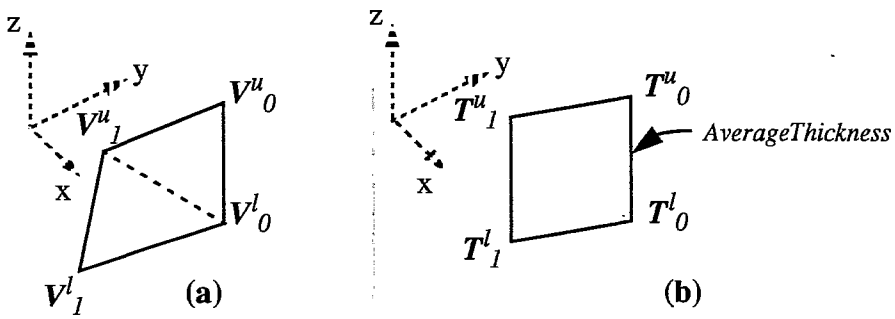


**Figure 6.6 Vertical area preservation technique.(a) Formed (initial)state; (b) Unformed (final) state.**

The remaining vertices of the two surfaces are then transformed by concentric layers propagating outwards from the starting point. Each layer is initialized by computing four reference points in the same manner as the four initial primary neighbors of the starting point. These reference points are topologically along the same *i*th line or *j*th column of the starting point. The remaining points in that layer are then calculated along a given *i*th line or *j*th column as long as there are at least three adjacent vertices already transformed (see Figure 6.7.)

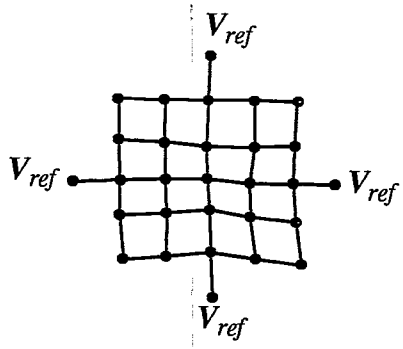


**Figure 6.7 Concentric mapping showing reference points.**

In most cases, along a given *i*th line or *j*th column, there are four adjacent vertices already mapped or transformed. In this situation the fourth overhanging vertex is ignored to prevent an imbalance that would be introduced by including it in the calculations [20] (see Figure 6.8.)

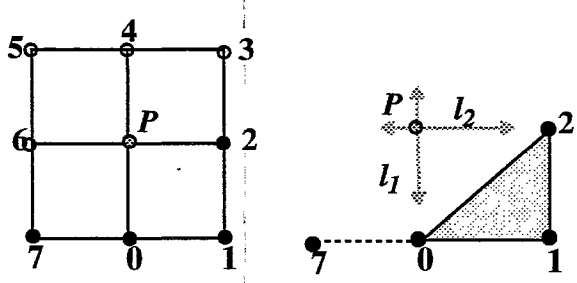


**Figure 6.8 Four neighbor case. Vertices 7, 0, 1 and 2 are mapped [20].**

## 6.5 Mapping Example

An example application is presented that demonstrates the differences between Nair's formulation (constant area transformation) and the present constant volume transformation algorithm. These example applications were run on a Silicon Graphics 200MHz R4400 workstation with 64MB of RAM.

As shown in Figure 6.9, a surface was constructed that resembles an actual deep drawing operation of a square box. This surface was represented by a 40 by 40 parametric subdivision. Due to the fact that only one NURBS surface was used to model the entire piece, the resultant surface was not exactly what one might get from drawing a square box but only an approximation.

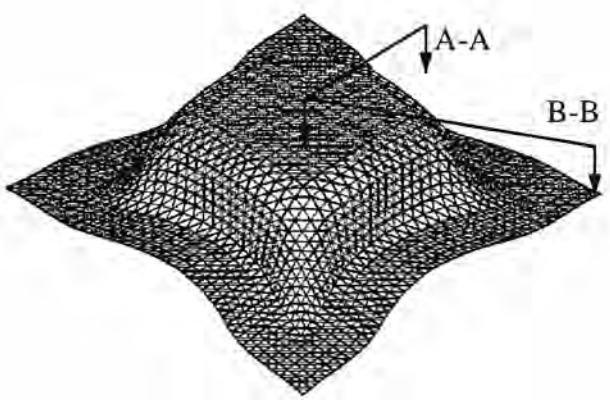


**Figure 6.9 B-Spline surface (top) and corresponding lower surface.**

### 6.5.1 Constant Area algorithm

This algorithm assumes an ideal process with no change in thickness. The resulting blank can be seen in Figure 6.10. Clearly the algorithm has some difficulties in the area calculations close to the corners of the surface. This is due to fact that the area loci are almost par-

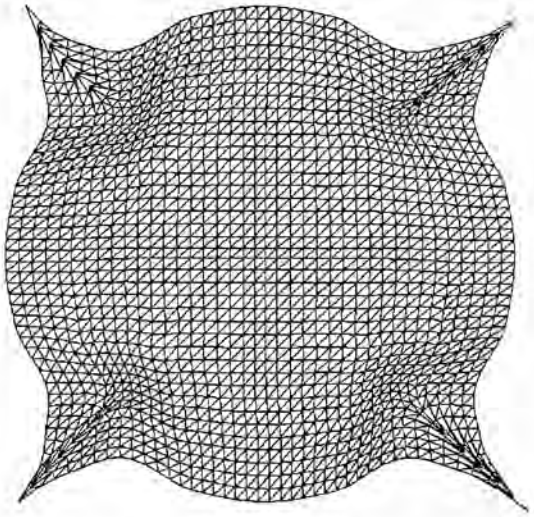

**Figure 6.10 Mapped surface, constant area transformation algorithm.**

allel in these regions resulting in floating point errors in finding the interception point. This algorithm does not account for the fact that in a real operation, the corners and the edges of the surface are necessarily thicker than the flange (vertical) areas or the corners of the box.

### 6.5.2 Constant Volume Algorithm

The thickness of the formed piece was estimated using information on thickness strains from a previous study done on this type of press forming, more specifically on the deep drawing of a square box using a modified finite element algorithm by Jiang and Lee [30]. As shown in Figure 6.9, along the section A-A and B-B, the computed thickness is based on the plots on Figure 6.11 and 6.12. The thickness at all the other points was interpolated from these values.

The resulting blank is shown in Figure 6.13. It more closely resembles a square blank, which was the initial assumption of this example. This algorithm especially handles better the calculations of the corners of the surface because of the added flexibility of the extra degree of freedom.

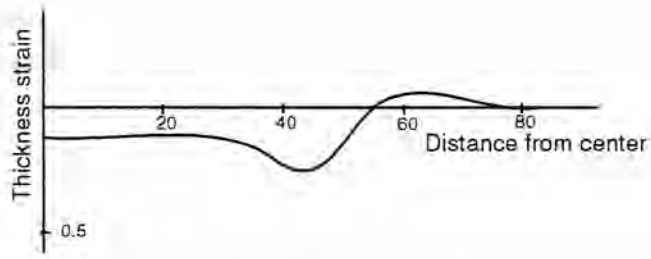


**Figure 6.11 Thickness strain distribution along the diagonal direction for the deep drawing of a square box (section B-B.) [30]**

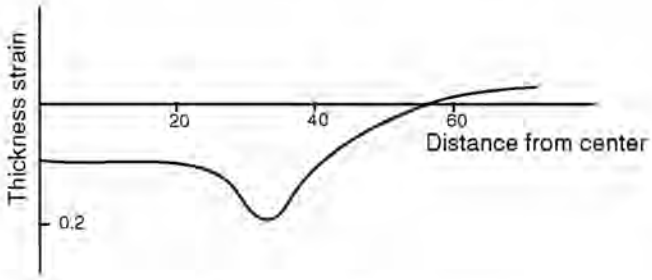


**Figure 6.12 Thickness distribution along the transverse direction for the deep drawing of a square box (section A-A.) [30]**

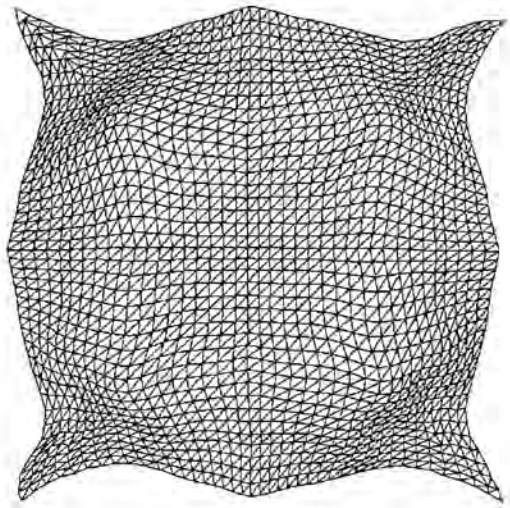

**Figure 6.13 Mapped surface, constant volume transformation algorithm.**

This example was used only to illustrate the differences between the two algorithms and the calculated blank is only the result of the hypothetical surface presented in Figure 6.9. It does not, however present any relation to the deep drawing of a square box studied by Jiang and Lee.

# 7. CONCLUSIONS AND FUTURE RESEARCH

## 7.1 Conclusions

Two major techniques that enhance the formability assessment tools developed by Nair were presented. The algorithms developed allow designers to interactively gather qualitative information about blank development in press forming. The first technique deals with the application of a modified constant area transformation technique to more complex surfaces common in industry. The second technique extends Nair's formulation by allowing thickness variations. An efficient algorithm for the calculation of geometric surface strains was presented and was used as a validation tool in Nair's constant area formulation and the new techniques introduced in this research. This algorithm used an approach based mostly on Marciniak's studies on surface strains as opposed to the technique presented by Nair which was solely based on Sowerby's model.

These new algorithms addressed some of the problems encountered by Nair. The multi-peak technique provides more flexibility when dealing with geometrical shapes that have several peaks. The volume conservation technique is a natural extension of Nair's formulation and possesses most of the attractive properties of the constant area transformation such as linear time complexity and no dependence on material properties. It is, however, more realistic since it takes into account the fact that in most cases, the sheet does not maintain its thickness throughout the entire workpiece during the forming process. The calculated values of geometric surface strains are a good indicator of the amount of shear involved in the process and can be used to determine regions where fracture might occur.

## 7.2 Future Research

Research in this field is continuing by trying to join both of the presented techniques into a single more complete assessment tool. The first step, however, is to incorporate more accurate thickness information into the volume conservation technique for several types of shapes. It is also hoped that the presented mapping strategy can be improved by using irregular meshes and multiple surface descriptions, thus being able to handle more complex and realistic surfaces.

# APPENDIX . DETAILS OF GEOMETRICAL STRAINS CALCULATION

The $(u_1, u_2)$ coordinates of the deformed grid need to be determined in order to obtain the strain coefficients seen in chapter 5. For that purpose, the set of arbitrary coordinate axes $OU_1$ and $OU_2$ (see figure 5.2(b)) was chosen in the deformed shape (which is the input shape in the algorithms presented in this thesis) according to figure 1. The axis $OU_1$ was chosen has

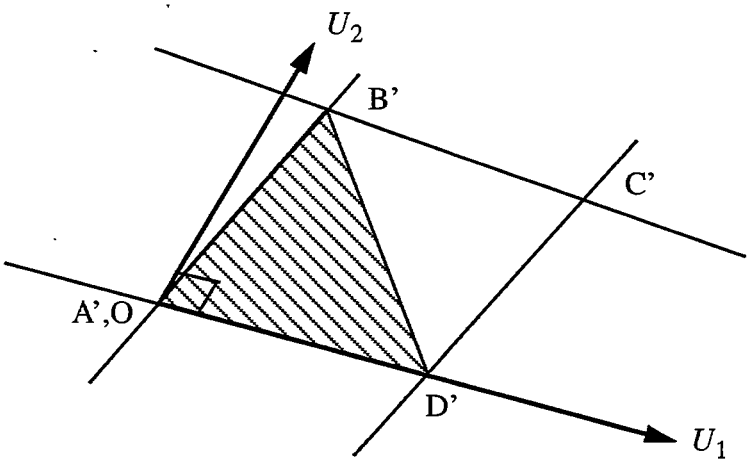


**Figure A1 Deformed grid measured in the $U_1$, $U_2$ frame.**

the direction of OD' with the axis $OU_2$ lying on the same plane as the triangle D'A'B'. The $(u_1, u_2)$ coordinates of B' and D' are therefore given by

$$\begin{aligned} u_1(\mathrm{D}') &= |\mathrm{OD}'| \\ u_2(\mathrm{D}') &= 0 \\ u_1(\mathrm{B}') &= |\mathrm{OB}'|\cos\theta \\ u_2(\mathrm{B}') &= |\mathrm{OB}'|\sin\theta \end{aligned} \tag{0.1}$$

where $\theta$ is the intended angle between OD' and OB'. The same calculation was performed for the upper triangle in figure 1 using vertices B', C' and D'. The resulting strain values for the

quadrilateral formed by A', B', C' and D' were averaged from the two triangles. Those are the values shown in figure 5.3 and figure 5.4.

# REFERENCES


[1] Sachs, G., 1934-5, "New Researches on the Drawing of Cylindrical Shells," *Proc. Inst. Automobile Engineers*, London, pp. 588-600.

[2] Willis, J., 1954, *Deep Drawing*, Butterworths, London.

[3] Hill, R., 1950, *The mathematical Theory of Plasticity*, Oxford University Press, Oxford.

[4] Yoshida, K., and Miyauchi, K., 1977, "Experimental Studies of Material Behavior as Related to Sheet Metal Forming," *Mechanics of Sheet Metal Forming*, Plenum Press, New York, pp. 19-52.

[5] Keeler, S.P., 1965, "Determination of Forming Limits in Automotive Stampings," *Society of Automotive Engineers*, Paper No. 650535.

[6] Barata da Rocha, A., Barlat, F., and Jalinier, J.M., 1985, "Forming Limits of Anisotropic Sheets in Complex Strain Paths," *Proceedings of the symposium on Computer Modeling of Sheet Metal Forming Processes,* sponsored by The Metallurgical Society, held at the 12th annual Automotive Material Symposium, Ann Arbor, Michigan, pp. 93-106.

[7] Anand, K.G., Zhao, D., Yu, C.J., Rammarayan, V., and Chaudhury, P.K., 1993, "Forming Limit Diagrams of Titanium Sheets," *Proceedings of a symposium on Computer Applications in Shaping & Forming of Materials*, sponsored by the Shaping and Forming Committee, held at the Annual Meeting of The Minerals, Metals & Materials Society, Denver, Colorado, February 21-25, 1993, pp. 231-238.

[8] Tozawa, Y., 1977, "Plastic Deformation Behavior Under Conditions of Combined Stress," *Mechanics of Sheet Metal Forming*, Plenum Press, New York, pp. 81-110.

[9] Hutchinson, J.W., Neale, K.W., and Needleman, A., 1977, "Sheet Necking-I. Validity of Plane Stress Assumptions of the Long-Wavelength Approximation," *Mechanics of Sheet Metal Forming*, Plenum Press, New York, pp. 111-126.

[10] Wagoner, R.H., 1985, "Constitutive Equations for Sheet Forming Analysis," *Proceedings of the symposium on Computer Modeling of Sheet Metal Forming Processes,* sponsored by The Metallurgical Society, held at the 12th annual Automotive Material Symposium, Ann Arbor, Michigan, pp. 77-92.

[11] Needleman, A., and Rice, J.R., 1977, "Limits to Ductility Set by Plastic Flow Localization," *Mechanics of Sheet Metal Forming*, Plenum Press, New York, pp. 237-267.

[12] Onate, E., and Saracibar, C.A., 1992, "Numerical Modelling of Sheet Metal-Forming Problems," *Numerical Modelling of Material Deformation Processes*, Springer-Verlag, London, pp. 318-357.

[13] Zhou, D., and Wagoner, R.H., 1993, "Application of a New Algorithm in Sheet Forming Simulation," *Proceedings of a symposium on Computer Applications in Shaping & Forming of Materials*, sponsored by the Shaping and Forming Committee, held at the Annual Meeting of The Minerals, Metals & Materials Society, Denver, Colorado, February 21-25, 1993, pp. 41-52.

[14] Pasquinelli, G., 1992, "An Algorithm to Model the deep Drawing Process by the Finite-Element Method," *Proceedings of the NUMIFORM' 92 conference*, Valbonne, France, September 14-18, 1992, pp. 287-292.

[15] Karima, M., 1989, "Blank Development and Tooling Design for Drawn Parts Using a Modified Slip Line Field Based Approach," *Journal of Engineering for Industry*, Vol. 111, No. 11, pp. 345-350.

[16] Bramley, A.N., and Osman, F.H., 1992, "The Upper Bound Method," *Numerical Modelling of Material Deformation Processes*, Springer-Verlag, London, pp. 114-130.

[17] Kokkonen, V., 1985, "Modeling of Forming Processes for Tool Design and Manufacturing at Volvo," *Proceedings of the symposium on Computer Modeling of Sheet Metal Forming Processes,* sponsored by The Metallurgical Society, held at the 12th annual Automotive Material Symposium, Ann Arbor, Michigan, pp. 13-20.

[18] Demeri, M.Y., 1993, "Drawbeads in Sheet Metal Forming Simulation," *Proceedings of a symposium on Computer Applications in Shaping & Forming of Materials*, sponsored by the Shaping and Forming Committee, held at the Annual Meeting of The Minerals, Metals & Materials Society, Denver, Colorado, February 21-25, 1993, pp. 301-310.

[19] Majlessi, S.A., and Lee, D., 1987, "Further Developments of Sheet Metal Forming Analysis Method," *Journal of Engineering for Industry*, Vol. 109, No. 11, pp. 331-337.

[20] Nair, N., 1993, "Development of Manufacturability Constraints for Press Forming of Sheet Metal Components," *Master's Thesis*, Iowa State University.

[21] Gerdeen, J.C., and Chen, P., 1989, "Geometric Mapping Method of Computer Modelling of Sheet Metal Forming," *Proceedings of the NUMIFORM'89 conference*, Fort Collins, Colorado, pp. 437-444.

[22] Chu, E, Soper, D., Gloekl, H., and Gerdeen, J.C., 1985, "Computer-Aided Geometric Simulation of Sheet Metal Forming Processes," *Proceedings of the symposium on Computer Modeling of Sheet Metal Forming Processes,* sponsored by The Metallurgical Society, held at the 12th annual Automotive Material Symposium, Ann Arbor, Michigan, pp. 65-76.

[23] Blount, G.N., and Stevens, P.R., 1990, "Blank Shape Analysis for Heavy Gauge Metal Forming," *Journal of Materials Processing Technology*,

[24] Hosford, W.F., and Cadell, R.M., 1983, *Metal Forming, Mechanics and Metallurgy*, Prentice-Hall inc., Englewood Cliffs, New Jersey.

[25] Love, A.E.H., 1944. *A Treatise on the Mathematical Theory of Elasticity*, Dover Publications, New York.

[26] Dinda, S., James, K.F., Keeler, S.P., and Stine, P.A., 1981, *How to Use Circle Grid Analysis for Die Tryout*, American Society of Metals, Metal Park, Ohio.

[27] Sowerby, R., Chu, E., and Duncan, J.L., 1982, "Determination of Large Strains in Metal Forming," *Journal of Strain Analysis*, Vol. 17, No. 2, pp. 95-101.

[28] Marciniak, Z., and Duncan J.L., 1992, *The Mechanics of Sheet Metal Forming*, Edward Arnold, U.K.

[29] Piegl, L., and Tiller, W., 1987, "Curves and Surface Construction Using Rational B-splines," *Computer-Aided Design*, Vol. 19, No. 9, pp. 485-497.

[30] Jiang, H. Y., and Lee, D., 1992, "Numerical Simulation of Sheet Metal Forming Processes Based on Large Deformation Shell Elements," *Proceedings of the NUMIFORM'92 conference,* Valbonne, France, pp.485-489.

[31] Batoz, J.L., Guo, Y.Q., Duroux, P., and Detraux, J.M., 1989, "Geometric Mapping Method of Computer Modelling of Sheet Metal Forming," *Proceedings of the NUMIFORM'89 conference*, Fort Collins, Colorado, pp. 383-388.

[32] Boeing Computer Services, 1994, *David Taylor Research Center Spline Geometry Library*, Carderock Division, Naval Surface Warfare Center, Bethesda, Maryland.

[33] Nair, N., and Oliver, J., 1993, "Area Preserving Transformation Algorithm for Press Forming Blank Development," *Proceedings of the 19th Annual ASME Design Automation conference*, Albuquerque, New Mexico, pp. 163-172.